Particle capture by drops in turbulent flow

Arash Hajisharifi
Department of Engineering and Architecture, University of Udine, 33100 Udine, Italy

Cristian Marchioli[*,†]
Department of Engineering and Architecture, University of Udine, 33100 Udine, Italy

Alfredo Soldati[‡]
Institute of Fluid Mechanics and Heat Transfer, TU Wien, 1040 Wien, Austria

(Received 9 October 2020; accepted 21 January 2021; published 5 February 2021)

We examine the process of particle capture by large deformable drops in turbulent channel flow. We simulate the solid-liquid-liquid three-phase flow with an Eulerian-Lagrangian method based on direct numerical simulation of turbulence coupled with a phase-field model, to capture the interface dynamics, and Lagrangian tracking of small (sub-Kolmogorov) particles. Drops have the same density and viscosity of the carrier liquid, and neutrally buoyant, quasi-inertialess, solid particles are one-way coupled with the other phases. Our results show that particles are transported towards the interface by jetlike turbulent motions and, once close enough, are captured by interfacial forces in regions of positive surface velocity divergence. These regions appear to be well correlated with high-enstrophy flow topologies that contribute to enstrophy production via vortex compression or stretching. Examining the turbulent mechanisms that bring particles to the interface, we have been able to derive a simple transport model for particle capture. The model is based on a single turbulent transport equation in which the only parameter scales with the turbulent kinetic energy of the fluid measured in the vicinity of the drop interface, and its predictions of the overall capture efficiency agree remarkably well with numerical results.

DOI: 10.1103/PhysRevFluids.6.024303

I. INTRODUCTION

The process of particle capture by drops or bubbles in a turbulent flow is of relevance in a number of industrial applications requiring particulate abatement, e.g., via wet scrubbing [1–3]. The very same process is also observed in environmental problems, such as accidental oil spills in which oil interacts with sediments to form oil-particle aggregates that may affect the transport of spilled oil and enhance oil biodegradation [4]. In these applications, particle capture occurs in two steps: First, particles move towards the drop or bubble surface under the influence of turbulence in the carrier liquid, possibly aided by external forces as in the case of electrostatic scrubbing [5,6]; then, particles stick to the drop or bubble surface upon inertial impaction or turbulent diffusion. Particle behavior upon impaction determines the overall attachment efficiency, which in turn affects the overall capture efficiency of the drop or bubble. In this context, a crucial physical property is surface

[*]Corresponding author: marchioli@uniud.it
[†]Also at Department of Fluid Mechanics, CSIM, 33100 Udine, Italy
[‡]Also at Department of Engineering and Architecture, University of Udine, 33100 Udine, Italy

tension, which controls drop or bubble deformability, drives particle adhesion, and leads to the formation of a layer that may change the mechanical and mass transport properties of the interface [7–9].

Particle capture and subsequent distribution on fluid interfaces of complex morphology are aspects of a multifaceted, multiphase flow problem, which must be investigated with a stepwise approach in order to unravel the physical mechanisms involved. The aim of this study is to elucidate the mechanisms that govern particle capture at the surface of a swarm of deformable drops transported by a turbulent flow, focusing in particular on the characterization of the flow events that bring particles to the surface. This interest is motivated by the need for detailed information about the near-interface flow field in usual engineering practice, e.g., for the development of physics-based models or correlations able to predict transfer rates across a liquid-liquid interface [10]. Currently, industrial computational fluid dynamics (CFD) tools can only rely on mechanistic correlations to predict the capture efficiency of full-scale equipment [10,11].

To study the targeted three-phase turbulent flow, we use a computational approach that couples the direct numerical simulation (DNS) of the carrier fluid and drops with an interface-capturing method for the evolution of the drop surface and a Lagrangian tracking method for the particle dynamics.

Three-phase computational models such as the one adopted here pose computational challenges in terms of modeling the interactions among the different phases and the complex dynamics produced by a moving, deformable interface [12]. Drops introduce additional physical mechanisms into the flow due to their ability to deform but also to breakup and coalesce with other drops, thus changing the overall surface area available for particle capture. The problem is complicated further by the wide range of length scales involved, from the interface thickness $O(10^{-9})$ m to the particle size $O(10^{-5})$ m to the drop size $O(10^{-2})$ m. Because of these complexities, most of the numerical studies available in the literature focus on the role that surface physicochemical forces have in determining particle adsorption in no-flow or viscous flow conditions, when particle-drop interactions are not affected by the flow hydrodynamics. Examples include the study of the behavior of a single particle trapped at a planar fluid interface [13,14], the surface stress tensor modification for a pendant drop covered by a monolayer of particles in the low-Reynolds-number limit [15], or the attachment of a colloidal particle to the surface of an immersed bubble rising in still fluid [16], to name a few recent works. Also relevant is the study by the authors of [17], who developed a discrete-element-method volume-of-fluid (DEM-VOF) approach to reproduce drop formation and interface perturbations from a single particle. The same methodology was applied in [18] to study gas-solid-liquid flows of relevance for sedimentation problems.

All of the above-mentioned studies have contributed to the physical understanding of particle-laden fluid interfaces, but do not consider turbulent flow conditions: Clearly, the flow hydrodynamics must be accounted for in turbulent systems, which are the focus of our investigation. Intuitively, one expects particles to be brought in the near-interface region by coherent jetlike fluid motions able to generate local deformations of the drop surface along the surface itself (via the tangential stress they generate) but also along the interface-normal direction (via the pressure fluctuations and normal stresses they induce). When strong enough, these deformations will produce a change in the topology of the flow surrounding each drop, as compared to the topology of an unladen flow [19], and will play a role in the particle adhesion process. To examine this role, we have concentrated our analysis on the fluid motions that occur in the proximity of the interface, where the smallest hydrodynamic length scales are typically located. For this purpose, we consider a density- and viscosity-matched flow that allows uncoupling of inertial effects associated with particle size from those due to differential density [20]. We also neglect particle-particle iterations of nonhydrodynamic origin (e.g., electrostatic interactions), which are crucial in determining particle behavior on the interface during the trapping stage but are negligible prior to capture [21]. Even in this simplified case, the presence of an interface is crucial as it represents an elastic, compliant boundary that can modulate the overall energy and momentum transfer of the carrier phase and the drops [22].

The paper is structured as follows. In Sec. II, the physical problem and the numerical methodology are presented: Specifically, we investigate the interaction between sub-Kolmogorov particles and super-Kolmogorov drops in a channel flow configuration, considering particles with low, albeit different, inertia. In Sec. III, first we characterize the flow topology near the locations of the interface at which particles get captured, by means of classical topology indicators [23]. Then, we examine the time evolution of the fraction of captured particles, proposing a simple predictive model to estimate the capture rate. Finally, in Sec. V, the main findings are summarized and future perspectives are provided.

II. PHYSICAL PROBLEM AND METHODOLOGY

The physical problem considered in this study consists of a turbulent three-phase channel flow in which large, deformable drops and small, spherical particles are transported by a carrier liquid. To numerically simulate this flow, we performed a direct numerical simulation (DNS) of the Navier-Stokes equations, which provides an accurate representation of turbulence, and used a phase-field method (PFM) to describe the dynamics of the drop surface (referred to as interface hereinafter) via the Cahn-Hilliard equations. Finally, we used a Lagrangian approach based on a suitably simplified version of the Maxey-Riley-Gatignol equation to compute the trajectory of the particles. Note that the Navier-Stokes equations, which define the hydrodynamics of the system, include an additional force term to account for the presence of the interface. In the following, the PFM is presented first and then the force coupling with the Navier-Stokes equations is described. Finally, the Lagrangian particle tracking is discussed.

A. Modeling of the interface dynamics

The phase-field method adopted in this study uses a scalar field (order parameter) to describe the transport of the phase field ϕ, which provides the instantaneous shape and position of the interface. The phase field is constant in the bulk of both the carrier phase ($\phi = -1$) and the drops ($\phi = +1$), while undergoing a smooth transition across the interfacial layer. The position of the interface is given by the isolevel $\phi = 0$. The time evolution of the order parameter ϕ is given by the Cahn-Hilliard equation, which reads, in dimensionless form,

$$\frac{\partial \phi}{\partial t} + \mathbf{u} \cdot \boldsymbol{\nabla} \phi = \frac{1}{\mathrm{Pe}_\phi} \nabla^2 \mu_\phi + f_p, \tag{1}$$

where $\mathbf{u} = (u, v, w)$ is the carrier fluid velocity field vector, Pe_ϕ is the Péclet number (ratio between the diffusive and convective timescale controlling the interface relaxation), μ_ϕ is the chemical potential, and f_p is a penalty flux (not accounted for in the standard phase-field formulation) introduced to force the interface toward its equilibrium by reducing the diffusive fluxes induced by the gradient of μ_ϕ [24–26]. Through this term, the equilibrium profile of the interface can be maintained and the drawbacks of the standard formulation (e.g., mass leakage) can be overcome. The penalty flux is defined as

$$f_p = \frac{\lambda}{\mathrm{Pe}_\phi} \left\{ \nabla^2 \phi - \frac{1}{\sqrt{2}\mathrm{Ch}} \boldsymbol{\nabla} \cdot \left[(1 - \phi^2) \frac{\boldsymbol{\nabla} \phi}{|\boldsymbol{\nabla} \phi|} \right] \right\}, \tag{2}$$

with the parameter λ set according to the scaling proposed in [25,26]. The Cahn number Ch represents the dimensionless thickness of the interfacial layer. The chemical potential μ_ϕ is defined as the variational derivative of the Ginzburg-Landau free-energy functional, $\mathcal{F}[\phi, \boldsymbol{\nabla}\phi]$. The functional is given by the sum of two different contributions:

$$\mathcal{F}[\phi, \boldsymbol{\nabla}\phi] = \int_\Omega (f_0 + f_m) d\Omega, \tag{3}$$

where Ω is the reference domain. The two contributions are defined as follows [27,28]:

$$f_0 = \frac{1}{4}(\phi - 1)^2(\phi + 1)^2, \tag{4}$$

$$f_m = \frac{\mathrm{Ch}^2}{2}|\nabla\phi|^2. \tag{5}$$

The term f_0 is the double-well potential that describes the tendency of the system to separate into two pure fluids; the term f_m is the mixing energy and accounts for the energy stored at the interface (i.e., the surface tension). The chemical potential is thus obtained as

$$\mu_\phi = \frac{\mathcal{F}[\phi, \nabla\phi]}{\delta\phi} = \phi^3 - \phi - \mathrm{Ch}^2\nabla^2\phi. \tag{6}$$

When the system is at equilibrium, the chemical potential is uniform over the entire domain. The equilibrium profile for a flat interface located at $s = 0$, with s being the coordinate normal to the interface, can be obtained by solving $\nabla\mu_\phi = 0$, which yields the following hyperbolic tangent profile:

$$\phi_{\mathrm{eq}}(s) = \tanh\left(\frac{s}{\sqrt{2}\mathrm{Ch}}\right). \tag{7}$$

This profile ensures a smooth transition between the limiting values $\phi = \pm 1$ that are reached in the bulk of each phase.

B. Hydrodynamics

The hydrodynamics of the three-phase flow is described by the continuity and Navier-Stokes equations, which are coupled with the Cahn-Hilliard equation previously introduced. This computational model can handle nonmatched properties in general cases [28,29]; density and viscosity can be defined as a function of the phase field ϕ, but in this study we assume the two Eulerian phases, namely, the carrier fluid (denoted by subscript f) and the drops (denoted by subscript d), to have matched density ($\rho = \rho_f = \rho_d$) and matched viscosity ($\eta = \eta_f = \eta_d$). From an applicative point of view, the matched-density assumption appears to be fully justified by the fact that we are interested in a liquid-liquid dispersion, while the matched-viscosity assumption appears to be relevant for situations in which the two fluids are water and low-viscosity silicone oil. For different combinations of immiscible fluids, the difference in viscosity would influence drop breakup and coalescence, thus introducing an additional complexity into the problem. As shown in [28], drops coalesce and break following a complex dynamics that is primarily controlled by the interplay between turbulence fluctuations (measured by the Reynolds number), surface tension (measured by the Weber number), and the viscosity ratio. Qualitatively, an increase of drop viscosity decreases the breakup rate, very much like an increase of surface tension does. Eventually, however, a steady state in the number of drops is always achieved, regardless of the viscosity difference: This is exactly the condition in which particles are injected into the flow.

According to this one-fluid formulation, the dimensionless continuity and Navier-Stokes equations read

$$\nabla \cdot \mathbf{u} = 0, \tag{8}$$

$$\frac{\partial \mathbf{u}}{\partial t} + \mathbf{u} \cdot \nabla\mathbf{u} = -\nabla p + \frac{1}{\mathrm{Re}_\tau}\nabla^2\mathbf{u} + \frac{\mathrm{Ch}}{\mathrm{We}}\frac{3}{\sqrt{8}}\nabla \cdot \tau_c, \tag{9}$$

where ∇p is the pressure gradient, which includes both the mean pressure gradient that drives the flow and the fluctuating part; $\mathrm{Re}_\tau = u_\tau h/\nu_f$ is the friction Reynolds number (based on the friction velocity $u_\tau = \sqrt{\tau_w/\rho_f}$, with τ_w the mean wall shear stress, the channel half height h, and the fluid kinematic viscosity ν_f); $\mathrm{We} = \rho_f u_\tau^2 h/\sigma$ is the Weber number, based on the surface tension σ of

a clean interface; and $\tau_c = |\nabla\phi|^2 I - \nabla\phi \otimes \nabla\phi$ is the Korteweg stress tensor, which accounts for the interfacial force induced on the flow by the occurrence of capillary phenomena due to nonlocal molecular interactions at the interface of the two immiscible liquid phases.

C. Lagrangian tracking and particle-interface interaction model

The motion of the particles is described by a set of ordinary differential equations for the particle velocity and position, which stem from the balance of the forces acting on the particles. Particles are assumed to be neutrally buoyant ($\rho_p = \rho_f$, no effect of gravity) and smaller in size than the Kolmogorov length scale. In this study, we considered two force contributions: the drag force and the capillary force that is exerted on the particles when they interact with the interface, thus allowing for particle adhesion. With the above assumptions, the Lagrangian equations of motion for the particles, in dimensionless vector form, read

$$\frac{\partial \mathbf{x_p}}{dt} = \mathbf{u_p}, \tag{10}$$

$$\frac{\partial \mathbf{u_p}}{\partial t} = \underbrace{\frac{\mathbf{u_{@p}} - \mathbf{u_p}}{\mathrm{St}}}_{\text{Drag force}} + \underbrace{\frac{6A}{\rho_p/\rho_f}\frac{\mathrm{Re}_\tau}{\mathrm{We}}\frac{\mathcal{D}}{{d_p}^3}}_{\text{Capillary force}}, \tag{11}$$

where $\mathbf{x_p}$ and $\mathbf{u_p}$ are the particle position and velocity, respectively; $\mathbf{u_{@p}}$ is the fluid velocity at particle position (obtained using a sixth-order Lagrange polynomials interpolation scheme); $\mathrm{St} = \tau_p/\tau_f$ is the Stokes number, with the ratio of the particle relaxation time $\tau_p = \rho_p d_p^2/18\mu_f$ (with d_p the particle diameter and μ_f the fluid dynamic viscosity) to the carrier fluid characteristic time $\tau_f = \nu_f/{u_\tau}^2$; and $\mathcal{D}$ is the interaction distance between the center of mass of the particle and the nearest zero-level point on the fluid interface, which defines the range of action of the capillary force. Particles are always in the Stokes regime. This was verified by measuring their Reynolds number, $\mathrm{Re}_p = |\mathbf{u_{@p}} - \mathbf{u}_p| d_p/\nu_f$, throughout the simulation: Re_p is always significantly smaller than unity and therefore the drag force acting on the particles follows the Stokes law.

The expression of the capillary force in Eq. (11) corresponds to the case of small spherical particles adsorbed at a fluid interface, and has been adopted in several previous studies to model particle-interface interactions [15,18,30]. Specifically, the dimensional expression of the force reads

$$\mathbf{F}_c = \begin{cases} \mathcal{A}\pi\sigma\mathcal{D}\mathbf{n} & \text{if } \mathcal{D} \leqslant d_p, \\ 0 & \text{if } \mathcal{D} > d_p, \end{cases} \tag{12}$$

where $\mathcal{A}$ is a dimensionless parameter that characterizes the magnitude of the capillary adhesion force (incorporating the effect of the contact angle θ between the particle and the interface as well as the effect of the particle-to-drop size ratio), and $\mathbf{n}$ is the normal unit vector pointing from the particle center of mass to the zero-level set of ϕ. From Eq. (12), it is clear that $\mathbf{F}_c$ reproduces the effect of a potential well centered at the interface that favors particle adhesion and attachment to the surface of the drop as soon as the particle touches the interface. Albeit based on a mechanistic (rather than physics-based) model of the capillary force, Eq. (12) represents the state of the art as far as particle-interaction models are concerned [15].

The value of the parameter $\mathcal{A}$ is chosen to satisfy the condition that the adsorption energy $E_{\mathrm{ads}} = \pi\sigma r^2(1 - |\cos\theta|)^2$, which corresponds to the difference between the energy of a particle fully displaced from the interface into the bulk phase and the energy of the particle settling at equilibrium at the interface, balances the desorption energy $E_{\mathrm{des}} = \frac{1}{2}\mathcal{A}\pi\sigma r^2$, which corresponds to the energy required for particle detachment from the interface [21,30]. Note that the expressions for E_{ads} and E_{des} are exact for an isolated, chemically homogeneous spherical particle on a flat surface [21]. Assuming a contact angle $\theta = 90^o$, this balance yields $\mathcal{A} = 2$, which is the value used in our simulations. Additional runs for different values of $\mathcal{A}$ (specifically, $\mathcal{A} = 0.01$ and 0.1) were also performed to assess the effect of a change in the magnitude of $\mathbf{F}_c$ on the capture process. As far as

the statistical quantities discussed in Sec. III are concerned, no major effect was observed (small quantitative modifications).

We remark that in this study, only particles with tiny inertia are considered. For these particles, unsteady forces, such as added mass and lift, can be neglected with respect to drag without introducing major inaccuracies in the description of particle motion. In particular, when forces are expressed in wall units (indicated by superscript $+$), the ratio of the added mass force to the drag force scales as $F_{AM}/F_D \sim \mathrm{St} \cdot (\rho_f/\rho_p)$ while the ratio of the lift force to the drag force scales as $F_L/F_D \simeq \sqrt{\nu_f(\frac{\rho_f}{\rho_p})\mathrm{St}} \cdot \sqrt{\frac{\partial u_i^+}{\partial x_j^+}}$. Since St is small in our problem (see Sec. II E), it compensates the effect of large velocity gradients and, therefore, minor modifications of particle trajectories within the carrier fluid should be expected from inclusion of these two forces in Eq. (11). In fact, particles nearly behave as fluid tracers as long as they are brought about by the carrier fluid. Once they reach the near-interface region, the capillary force is expected to be dominant over the other forces (drag, in particular), thus favoring particle adhesion. However, this process may be significantly affected by the turbulence in the bulk of the carrier fluid, which tends to continuously deform the interface and modify the topology of the flow structures with which the particles interact as they approach the drop. Our aim is precisely to highlight the role played by these local flow structures and quantify their effect on particle adhesion.

D. Numerical method

The governing equations (1), (8), and (9) are solved numerically using a pseudospectral method that transforms the field variables into wave space. Specifically, Fourier series are used to discretize the variables in the homogeneous directions (streamwise x and spanwise y), while Chebychev polynomials are used in the wall-normal direction, z. The Helmholtz-type equations so obtained are advanced in time using an implicit Crank-Nicolson scheme for the linear diffusive terms and an explicit two-step Adams-Bashforth scheme for the nonlinear terms. Timewise, the Cahn-Hilliard equation is discretized using an implicit Euler scheme, which allows for the damping of unphysical high-frequency oscillation that may arise from the occurrence of steep gradients in the phase field [31,32]. All unknowns (velocity and phase field) are Eulerian fields defined on the same Cartesian grid, which is uniformly spaced in x and y and suitably refined close to the wall along z by means of Chebychev-Gauss-Lobatto points. Note that the Navier-Stokes equations are solved in their velocity-vorticity formulation and, therefore, are recast in a fourth-order equation for the wall-normal component of the velocity and a second-order equation for the wall-normal component of the vorticity. The Cahn-Hilliard equation is split into two second-order equations. Further details on the numerical method can be found in [36].

As far as boundary conditions are concerned, periodicity is imposed on all variables in x and y, whereas a no-slip condition for velocity is enforced at the two walls, located at $z/h = \pm 1$,

$$\mathbf{u}(z/h = \pm 1) = 0. \tag{13}$$

This condition yields the no-flux condition $\partial w/\partial z = 0$ for the wall-normal velocity at $z/h = \pm 1$. The same condition is applied to the phase field,

$$\frac{\partial \phi}{\partial z}(z/h = \pm 1) = 0, \quad \frac{\partial^3 \phi}{\partial z^3}(z/h = \pm 1) = 0. \tag{14}$$

These boundary conditions lead to the conservation of the integral of the phase field over time [32],

$$\frac{\partial}{\partial t} \int_\Omega \phi d\Omega = 0. \tag{15}$$

We remark here that the total mass of the carrier fluid and of the drops is conserved at all times, yet mass conservation of each phase is not guaranteed. To limit interphase mass leakage,

we adopted the flux-corrected formulation proposed in [24–26]. In the simulations discussed here, this formulation limits mass leakage to roughly 5% of the drops during the initial time transient. At the steady state, namely, when the particles are also injected into the flow (see next paragraph), mass leakage vanishes.

As far as the Lagrangian tracking is concerned, the particle equations of motion are integrated in time using an explicit Euler scheme. Particles are injected into the flow once the surface area of the drops has reached a steady state: Particles are initially placed at random locations within the volume occupied by the carrier fluid, namely, in regions of the flow where $\phi = -1$ to avoid direct injection inside a drop, with initial velocity $\mathbf{u}_p(\mathbf{x}_p, t_{\rm tr} = 0) = \mathbf{u}_{@p}(\mathbf{x}_p, t_{\rm tr} = 0)$, where $t_{\rm tr}$ is the particle tracking time. Interpolation of the flow variables (in particular, fluid velocity components and phase field) at the particle position is performed using fourth-order Lagrange polynomials.

E. Simulation setup

The flow is driven by a constant pressure gradient imposed along the streamwise direction, at shear Reynolds number $\mathrm{Re}_\tau = 150$ (corresponding to a Reynolds number $\mathrm{Re}_H \simeq 9000$ based on the hydraulic diameter). This value of the Reynolds number was chosen in view of the computational cost required to simulate the targeted three-phase system, characterized by a marked separation between the large scales in the bulk of the flow with the small scales generated near the deformable interface. To reproduce these scales with adequate accuracy, the grid resolution has to be much finer than that required by a single-phase flow [22]. Considering also that we must account for a third phase, we decided to choose a relatively low value of Re_τ, yet sufficient to produce a fully turbulent flow field [33–35]. Even at this low value of Re_τ, the entire simulation campaign required nearly 6×10^6 CPU hours on a large-scale parallel Tier-0 infrastructure with a raw data production of about 8 TB.

The computational domain consists of a closed-channel configuration with dimensions $L_x\times L_y\times L_z = 4\pi h\times 2\pi h\times 2h$ ($L_x^+\times L_y^+\times L_z^+ = 1885\times 942.5\times 300$ in wall units). This domain is discretized using $N_x\times N_y\times N_z = 512\times 256\times 257$ grid points, which provide an extremely well resolved turbulent flow field compared to the single-phase case (grid spacings are $\Delta x^+ = \Delta y^+ = 3.7$, $\Delta z^+_{\rm wall} = 0.0113$, and $\Delta z^+_{\rm center} = 1.84 \simeq \eta^+_{K,\rm center}/2$, with $\eta^+_{K,\rm center}$ the Kolmogorov length scale in the channel center) and has proven sufficient to describe the near-interface scales [22].

We considered two different values of the surface tension corresponding to $\mathrm{We}_L = 0.75$ and $\mathrm{We}_H = 1.5$, respectively. These values match those commonly found in oil-water mixture [37]. In Sec. III, the simulation results are discussed with reference to We_L, which corresponds to less deformable drops. However, we remark here that the effect of the Weber number observed in our simulations is limited to minor quantitative modification of the statistics examined. For the phase field, the value of the Cahn number has been set to ensure that there are at least five grid points across the interfacial layer to accurately resolve all the gradients occurring there [22,36]. This condition yields $\mathrm{Ch} = 0.02$. The Péclet number has been set according to the scaling $\mathrm{Pe}_\phi = 1/\mathrm{Ch} = 50$ proposed in [38] to achieve the convergence to the sharp interface limit.

At the beginning of the simulations, the phase field was initialized to generate a regular array of 256 spherical drops with normalized diameter $d/h = 0.2$ (corresponding to $d^+ = 60$ in wall units) that are injected in a fully developed turbulent flow. As mentioned, particles were released into the flow only after the surface area of the drops had reached a steady state, which results from a balance between coalescence and breakup events for the range of Weber numbers considered in this study. A total of five sets of $\mathcal{N}_p = 10^6$ particles at varying Stokes number were tracked: tracer particles ($\mathrm{St} = 0$), which are used as markers to sample all flow regions in the carrier fluid domain, and particles with $\mathrm{St} = 0.1$, 0.2, 0.4, and 0.8, corresponding to particle diameters much smaller than the drop diameter, $d_p/d \simeq O(10^{-2})$, at least.

Since the focus of the present study is on particle capture by turbulence, and given that the average particle volume fraction is $\Phi_V \sim O(10^{-4})$, the feedback of particles on the flow field is

not considered (one-way coupling simulation). Particles are characterized by low values of inertia and exhibit a weak tendency to cluster before being captured at the interface: This keeps the volume fraction low also locally, leading to a spatial distribution within the carrier fluid domain that remains dilute over the entire simulation. The neglect of two-way coupling effects is further justified in view of the low momentum that the neutrally buoyant particles can exchange with the fluid as compared to heavy particles. For the same reasons (low inertia and low volume fraction), particle-particle collisions are not accounted for: these are assumed to be negligible prior to particle adhesion to the drop interface and are expected to play a role only during the subsequent trapping stage, when particles are bound to move on a two-dimensional surface.

III. RESULTS AND DISCUSSION

In this section, we will first characterize the process of particle capture at the drop interface, focusing in particular on the topology of the flow structures that drive particle adhesion. Then, we will discuss the macroscopic outcome of this process, the time accumulation of particles on the interface, and propose a simple model to estimate the rate at which this accumulation takes place.

Particle capture and flow topology

A qualitative rendering of the instantaneous flow field is provided in Fig. 1, where a close-up view of one capture event is also shown. The carrier phase is rendered by means of the fluid streaklines. Drops are visualized by the $\phi = 0$ isosurface and are colored by the local curvature of the surface (concave areas with high negative curvature are shown in blue; convex areas with high positive curvature are shown in red). Particles are represented as blue dots, with size equal to the particle diameter (St $= 0.1$ particles are considered here). Note that after capture, particles remain trapped on the interface and tend to form filamentary clusters, which result from the action of the capillary force $\mathbf{F}_c$. The mechanisms that lead to the formation of these clusters and their topological characterization are beyond the scope of this paper, and will be the subject of an independent study focusing on particle dynamics after capture. It suffices to say here that the formation of neat particle filaments is favored by the neglect of interparticle collisions, which are expected to smear out densely concentrated clusters.

Two close-up views are provided: One (marked as *I*) shows a near-drop region of the flow populated by a swarm of particles that is being pushed toward the drop by the carrier fluid, the other (marked as *II*) shows one isolated particle approaching the interface with the order parameter distribution in the background. On the right end of the inset, this distribution (red line) is qualitatively compared with the distribution of the capillary force over the interaction distance $\mathcal{D}$: This force is zero everywhere except within a distance $\mathcal{D}$ from the interface, where its absolute value follows the blue line. At this time of the simulation, the total surface area of the drops has reached a statistically steady state that results from a balance of (now rare) coalescence and breakup events. Drop deformation induced by turbulence is apparent and is associated to a nonuniform distribution of the curvature, which can be computed starting from the phase field as

$$\kappa = -\boldsymbol{\nabla} \cdot \left(\frac{\boldsymbol{\nabla}\phi}{|\boldsymbol{\nabla}\phi|} \right) = -\frac{\nabla^2\phi}{|\boldsymbol{\nabla}\phi|} + \frac{1}{|\boldsymbol{\nabla}\phi|^2} \boldsymbol{\nabla}\phi \cdot \boldsymbol{\nabla}(|\boldsymbol{\nabla}\phi|). \tag{16}$$

In addition, the local unit vector $\mathbf{n}$ normal to each level-set curve is obtained as

$$\mathbf{n} = -\frac{\boldsymbol{\nabla}\phi}{|\boldsymbol{\nabla}\phi|}, \tag{17}$$

where Eqs. (16) and (17) are valid only if ϕ isosurfaces are parallel to each other. This property is conserved when advecting ϕ through the Cahn-Hilliard equation using the Pe $\propto$ Ch^{-1} scaling [38].

Focusing on inset *I*, we observe that particles tend to approach the drop and adhere to its surface in a convex region of the interface where curvature κ reaches a local peak. In this region, the flow

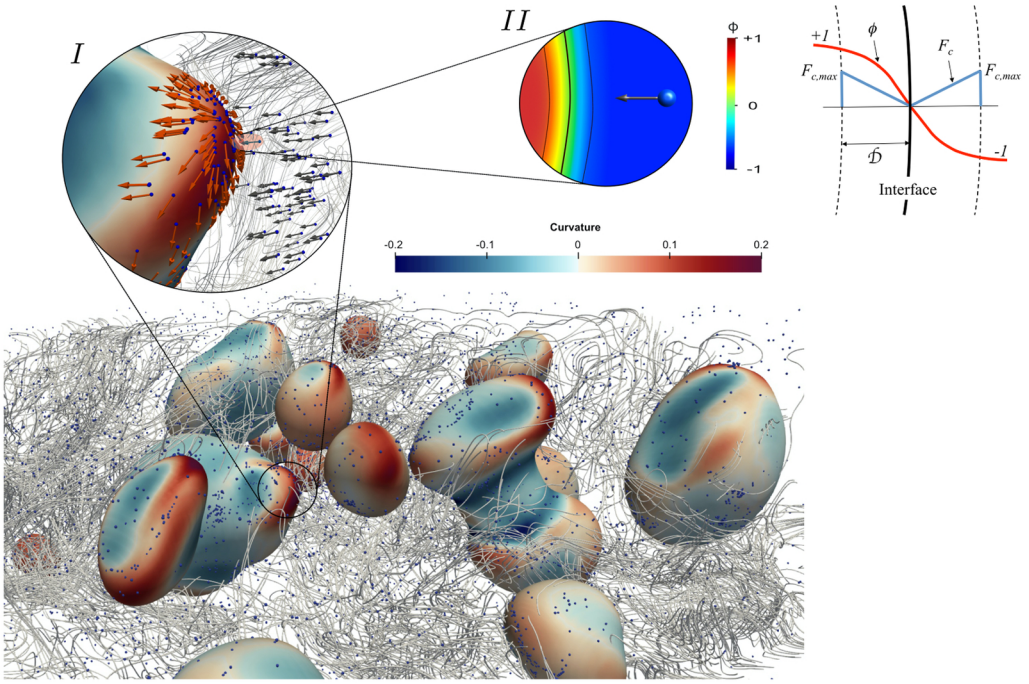

FIG. 1. Qualitative rendering of the flow configuration. Drops are colored by the local curvature of the interface, the flow field is rendered by the fluid streaklines, and particles are visualized as blue spheres. The insets provide close-up views of one particle capture event (inset *I*) and of one interface-approaching particle in isolation (inset *II*), respectively. Gray arrows represent the particle velocity magnitude and render the motion of particles that move towards the interface. Red arrows represent the interfacial stress sampled by the particles at the time of adhesion. The color map in the top inset shows the spatial distribution of the order parameter ϕ: The interface is located at $\phi = 0$ (thick black line). The thin black lines represent the fluid layer within which Φ transitions from $\phi = -1$ (fluid) to $\phi = +1$ (drop), as shown in the schematic on the right end of the inset, where the distribution of the capillary force F_c over the interaction distance $\mathcal{D}$ is also rendered. Note that $\mathcal{D}$ is shorter than the distance over which $-1 < \phi < +1$.

is impinging on the drop surface and the tangential shear stress is directed from the high-positive curvature region towards the neighboring, high-negative curvature regions. This anticipates that captured particles, while subject to the action of tangential stresses, will be driven toward such regions as long as they remain attached to the interface.

Figure 1 confirms the physical intuition that particles are brought in close proximity of the drop by coherent fluid motions that interact with the compliant drop surface. This interaction gives rise to highly nonuniform curvature and shear stress distributions. In order to examine these fluid motions in more detail, we consider first the two-dimensional fluid velocity divergence at the interface of the drop, referred to as surface divergence in the following. The surface divergence is defined as

$$\nabla_{2D} = \mathbf{n} \cdot \boldsymbol{\nabla} \times (\mathbf{n} \times \mathbf{u}). \tag{18}$$

According to this definition, particles captured at the surface probe a compressible two-dimensional system where regions of local flow expansion, generated by impinging fluid motions, are characterized by $\nabla_{2D} > 0$ and regions of local compression, generated by outward fluid motions, are characterized by $\nabla_{2D} < 0$.

In Fig. 2, we show the probability distribution function (PDF) of the surface divergence computed at the position occupied by the particles when they get captured by the interface. This position is

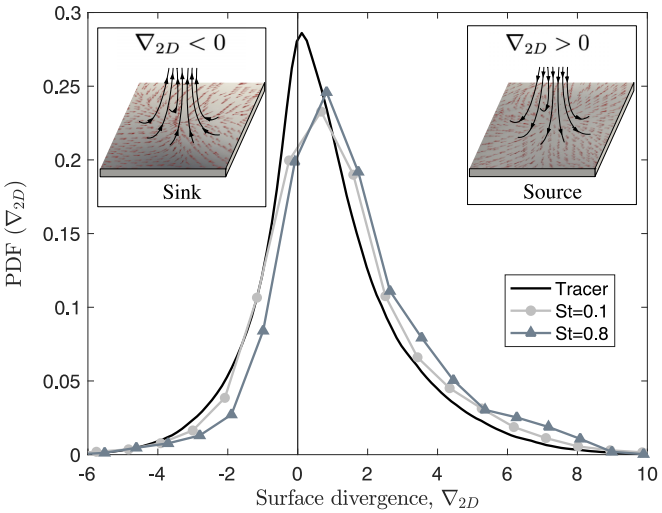

FIG. 2. PDF of the two-dimensional (2D) surface divergence, ∇_{2D}, seen by the particles when they get captured by the interface. Regions of local flow expansion (velocity sources) are characterized by $\nabla_{2D} > 0$; regions of local compression (velocity sinks) are characterized by $\nabla_{2D} < 0$. Symbols refer to simulation results (circles: St $= 0.1$, triangles: St $= 0.8$), whereas the solid line refers to the PDF computed for tracer particles uniformly distributed over the entire interface of each drop. The PDF was computed starting at time $t^+ \simeq 1000$ after particle injection and over a subsequent time interval $\Delta t^+ = 2000$.

evaluated at the time the particle touches the interface, namely, when the particle center is less than one radius away from the nearest zero-level point on the interface. To allow comparison among the different particle sets, we considered a reference distance equal to the radius of the largest particles (St $= 0.8$), which is equal to about one-tenth of the interface thickness and thus corresponds to a phase field $\phi = -0.71$. The PDFs for the St $= 0.1$ and St $= 0.8$ are shown and compared to the PDF obtained for the case of inertialess tracers uniformly distributed over the $\phi = -0.71$ isosurface. We remark that in our simulations, this is also the distance within which the capillary force $\mathbf{F}_c$ starts acting on the particle. Therefore, the PDFs shown in Fig. 2 are not affected by the model used for $\mathbf{F}_c$ in the equation of particle motion.

Figure 2 shows that in the case of the tracers, the PDF exhibits a clear peak at $\nabla_{2D} = 0$, but is also negatively skewed. This indicates that fluid motions directed towards the drop occupy a wider surface area compared to fluid motions directed away from the drop. The effect can be ascribed to the deformability of the interface, which is able to respond and adapt *elastically* to impinging flow events. In the case of particles with tiny inertia, the PDF shifts towards higher positive values of ∇_{2D}: The peak is now located at $\nabla_{2D} \simeq 1$, and inertia appears to play a negligible role for the range of Stokes numbers considered in the study. Overall, Fig. 2 corroborates the observation that particles tend to preferentially sample regions of local flow expansion as they attach to the drop. This already provides a first indication about the topological features of the flow near the interface.

To provide additional information about these features, we examine next the flow topologies that are sampled by the particles just before being captured. A flow topology analysis near deformable drops has been carried out recently in [19] for the case of decaying isotropic turbulence. Following the classification proposed in [39] (to which the reader is referred for a detailed discussion of the flow topologies in three-dimensional flow fields), these authors showed that there is a shift from high-enstrophy and low-dissipation structures favored outside the near-surface viscous layer to low-enstrophy and high-dissipation structures favored inside the viscous region and, eventually, to boundary-layer-like and vortex-sheet flow topologies at the surface. In close proximity of the surface, the observables examined to characterized the topological structures (the invariants of the

velocity gradients, rate-of-strain and rate-of-rotation tensors) exhibit statistical features that are very similar to those reported inside the viscous sublayer of wall-bounded turbulence [19,40]. The analysis we propose is thus justified by the expectation that the final particle capture rate will result from particle interaction with all these topological structures. To infer the local flow structures sampled by the particles, we use standard observables that are related to the invariants of the velocity gradients tensor $\mathcal{A} = [u_{i,j}]$ [23,41],

$$P = -\mathrm{tr}[\mathcal{A}], \tag{19}$$

$$Q = \tfrac{1}{2}(P^2 - \mathrm{tr}[\mathcal{A}^2]), \tag{20}$$

$$R = -\det[\mathcal{A}]. \tag{21}$$

For the present incompressible flow, $P = 0$ and the second invariant can be expressed simply as $Q = -\frac{1}{2}(S : S + \Omega : \Omega) = -\frac{1}{2}(S^2 + \Omega^2)$, where $S = \frac{1}{2}(u_{i,j} + u_{j,i})$ and $\Omega = \frac{1}{2}(u_{i,j} - u_{j,i})$ and the symmetric and antisymmetric components of $\mathcal{A}$, respectively. In this case, Q represents the local balance between vorticity (related to Ω) and strain rate (related to S). The flow topology parameter can now be introduced [22,42–44],

$$\mathcal{Q} = \frac{S^2 - \Omega^2}{S^2 + \Omega^2}. \tag{22}$$

Based on this definition, $\mathcal{Q} = 1$ corresponds to purely elongational flow ($\Omega = 0$), $\mathcal{Q} = 0$ corresponds to shear flow, and $\mathcal{Q} = -1$ corresponds to purely rotational flow ($S = 0$) [22]. The topology parameter has been used recently to examine the effect of a compliant interface on the flow field in different regions of the flow domain in two-phase systems [22,42,43]. We remark here that the turbulent flow field has lower intensity inside the droplets due to the elastic behavior of the interface, which damps convective effects and limits momentum transport from one fluid phase to the other [45]. This corresponds to smaller, nearly zero values of S and Ω that lead to frequent changes in the sign of the numerator of Eq. (22). In turn, these changes are amplified by the denominator, which is always definite positive and produces values of $\mathcal{Q}$ between -1 and $+1$, regardless of the specific value of S and Ω, namely, regardless of the turbulence intensity associated to these two tensors. To overcome this intrinsic limit of the above definition, we employed spline interpolation over neighboring grid points to smoothen the spatial distribution of $\mathcal{Q}$.

Figure 3 shows the instantaneous spatial distribution of $\mathcal{Q}$ in the wall-parallel $x^+ - y^+$ plane at the center of the channel. The interface of the drops is represented by the black solid lines. Figure 3(a) refers to the entire $x^+ - y^+$ plane, whereas the two insets show, for $\mathrm{St} = 0.1$ and $\mathrm{St} = 0.8$, respectively, a close-up view of particle distribution along the surface of the drop pair highlighted in Fig. 3(a). The presence of the interface has a clear influence on the local flow behavior. The carrier phase appears to be characterized by large areas of shear flow (in green, corresponding to values of $\mathcal{Q}$ close to zero) and smaller fragmented regions of rotational flow (in blue, corresponding to values of $\mathcal{Q}$ close to -1) and elongational flow (in red, corresponding to values of $\mathcal{Q}$ close to $+1$). The flow inside the drops, on the other hand, is most often characterized by the predominance of both shear and elongational flow regions, as also noted in [22]. The insets show that small changes of particle inertia are sufficient to modify the spatial distribution of the captured particles over the interface. Note that for the Weber number values considered in this study, only a small number of drops is found at the steady state: therefore, the drop size is large enough to minimize the internal flow confinement effects that are observed at higher Weber numbers [22].

It is not so easy to conclude something about the flow behavior very close to the interface just by visual inspection of Fig. 3. To this aim, in Fig. 4, we show the PDF of $\mathcal{Q}$ seen by the particles at the time they touch the interface and get captured. As done for Fig. 2, $\mathcal{Q}$ is evaluated when the phase-field value interpolated at particle position is $\phi = -0.71$, namely, at the edge of the capillary force range: This excludes any effect of this force on the motion of the particles in their final stretch to the interface. Lines and symbols are as in Fig. 2. For the case of inertialess tracers, the PDF is slightly asymmetric and negatively skewed, indicating that elongational flow

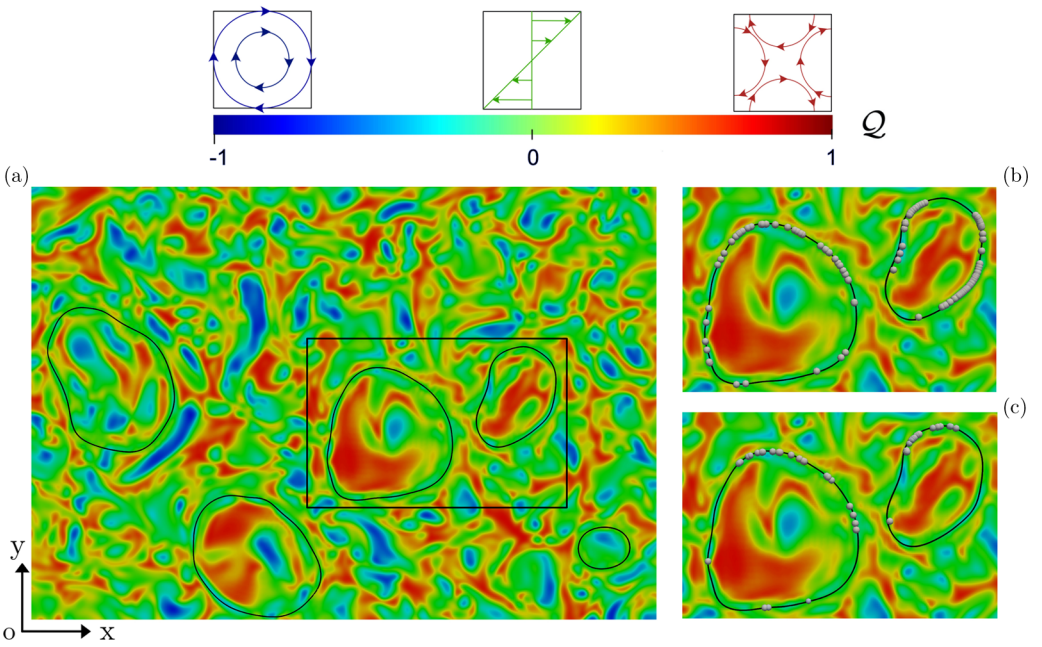

FIG. 3. (a) Flow topology parameter $\mathcal{Q}$ on the channel midplane ($x^+ - y^+$ plane); black solid lines identify the position of the drop interface (isolevel $\phi = 0$). (b), (c) Close-up view of the distribution of captured particles on the interface of the drop pair boxed in (a). Insets: (b) St $= 0.1$, (c) St $= 0.8$.

events ($\mathcal{Q} > 0$) are slightly more likely than rotational flow events ($\mathcal{Q} < 0$). Interestingly, a small deviation from the St $= 0$ limit is sufficient to produce a significant quantitative change in the shape of the PDF: This change is generated by the fact that particles can only reach the interface by following strong, coherent flow events directed towards the droplet, not because they can deviate from the fluid streamlines and touch the surface via a free-flight type of mechanism. Entrainment into these jetlike flow events, in turn, leads to a nonuniform spatial distribution of capture events on the interface and to a preferential sampling of the topological structures of the interface. Asymmetry

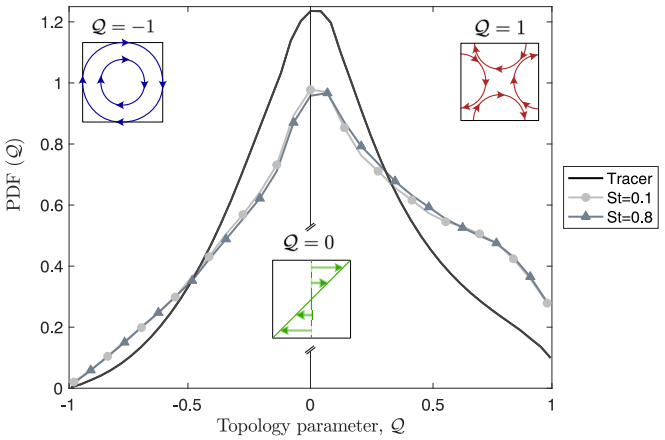

FIG. 4. PDF of the topology parameter, $\mathcal{Q}$, seen by the particles when they get captured by the interface. Lines and symbols are as in Fig. 2. The PDF was computed starting at time $t^+ \simeq 1000$ after particle injection and over a subsequent time interval $\Delta t^+ = 2000$.

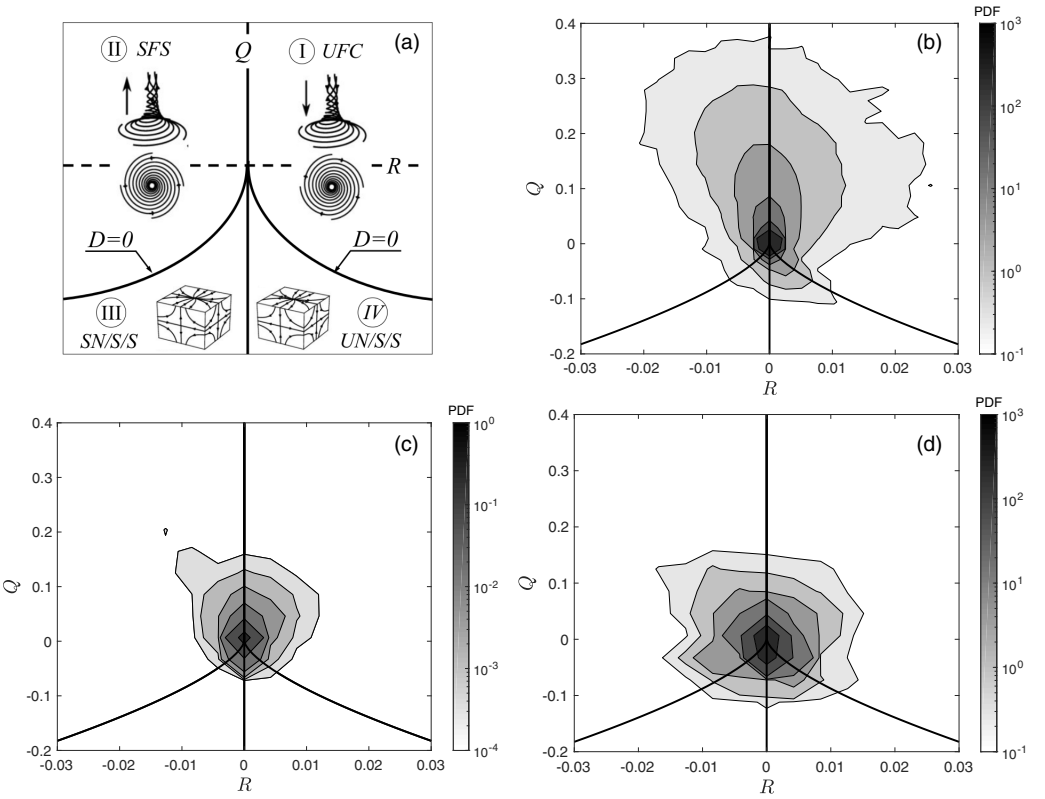

FIG. 5. (a) Incompressible flow critical point topologies according to the classification scheme in [23]: Topologies falling in region *I* are called unstable focus/compressing (UFC), while those falling in region *II* are called stable focus/stretching (SFS). Topologies falling in region *III* are called stable node/saddle/saddle (SN/S/S), while those falling in region *IV* are called unstable node/saddle/saddle (UN/S/S). Further critical points can be identified along the Q axis and the $D = 0$ line, but their characterization is beyond the scope of this study. (b)–(d) Joint PDF of Q, R conditionally sampled for fluid (b) at grid points over the entire interface of the drops, (c) at the position of the $\mathrm{St} = 0.1$ particle when they get captured, and (d) at the position of the $\mathrm{St} = 0.8$ particles when they get captured.

is increased and the likelihood of particles sampling shear-dominated flow events decreases in favor of elongation-dominated events. As particles reach the very-near-interface region, the interplay between the impinging fluid motions that are transporting the particles and the blockage effect of the interface generates stronger tangential stresses, which in turn generate localized elongational flows similar to that highlighted in inset *I* of Fig. 1. Strong rotational flow events also become slightly more likely, but this seems to be a minor effect.

To conclude the analysis of the flow events that drive particle capture, we examine their topological features by discussing the joint PDF of the second and third invariants of the velocity gradient tensor, Q and R. These invariants are computed at the Eulerian grid points and then interpolated at the instantaneous position of particle capture using fourth-order Lagrange polynomials: Near the interface, a one-sided version of the scheme is used to avoid mixing drop- and carrier-fluid velocities [19]. The time window considered to compute the invariants covers the last 400 viscous units of the simulations. The conditioned joint PDFs so obtained are shown in Fig. 5. For clarity of presentation, in Fig. 5(a), we show first a compact classification of all incompressible flow topologies in the (Q, R) plane [39,41]. This classification also involves the discriminant $D = \frac{27}{4}R^2 + Q^3$ of the velocity

TABLE I. Probabilities representing the tendency of captured particles to sample the different incompressible topologies near the interface of the drops. Probabilities are averaged over the last 400 viscous time units of the simulations.

Quadrant Topology	*I* Unstable focus/compressing	*II* Stable focus/stretching	*III* Stable node/saddle/saddle	*IV* Unstable node/saddle/saddle
Tracers	35%	45%	7%	13%
St = 0.1	42.5%	34.5%	9%	14%
St = 0.8	25%	33%	15%	27%

gradient tensor: If $D > 0$, then the tensor has one real and two complex-conjugate eigenvalues, indicating the prevalence of enstrophy in the flow; if $D < 0$, then the tensor has three real, distinct eigenvalues, indicating the prevalence of dissipation in the flow; if $D = 0$, then the tensor has three real eigenvalues, two of which are equal [19]. Based on the sign of D and R, four topological regions can be identified: When $D > 0$ and $R > 0$ (region I), the flow is characterized by a predominance of vortex compression over vortex stretching, and the opposite is true when $D > 0$ and $R < 0$ (region II); when $D < 0$ and $R < 0$ (region III), the flow is connected to diverging fluid trajectories, while being connected to converging trajectories when $D < 0$ and $R > 0$ (region IV).

Figure 5(b) shows the joint PDF conditioned at the position of uniformly distributed tracers. This PDF is characterized by the same teardrop shape that is typically observed in wall-bounded flows, and particularly in the viscous sublayer region. There is also evidence of events clustered around $Q = 0$ and $R = 0$, which are indicative of boundary-layer-like flow topologies [19]. This confirms that at least from a qualitative viewpoint, there are similarities between the flow field near a compliant interface and the flow field near a solid wall. The most probable flow topologies are those falling in regions I and II, as also shown in Table I: These topologies represent vortical motions that contribute to the production of enstrophy via vortex compression or stretching, respectively.

When we consider the joint PDF conditioned at the particle position, there is a clear change of shape. Comparing also the percent values reported in Table I, we observe a nontrivial effect of the Stokes number. For the St = 0.1 particles, we find an increased probability associated to unstable focus/compressing topologies and a nearly equivalent decrease of the probability associated to stable focus/stretching topologies with respect to tracers (the sum of the two probabilities being equal to 77%). This indicates that St = 0.1 particles sample preferentially fluid motions that contribute to enstrophy production via vortex compression more often than via vortex stretching. Fluid motions characterized by high strain and high dissipation are avoided by these particles. For the St = 0.8 particles, probabilities are more evenly distributed with a significant increase for the case of node/saddle/saddle topologies, particularly unstable ones. These are regions with large negative values of Q and represent sites of high dissipation that St = 0.8 particles apparently sample just before adhesion.

Overall, Figs. 4 and 5 indicate that particle capture occurs mostly in regions of local interface stretching produced by turbulent fluctuations normal to the interface within the carrier fluid. These regions correlate well with high-enstrophy flow topologies and are produced by a competition between shear-dominated and elongation-dominated events.

IV. PARTICLE CAPTURE RATE

The phenomenology of particle capture by the drop is as follows: A flow event, roughly described as a jet, transports the particles towards the interface; near the interface, the jet deflects and particles that are close enough are captured by the interfacial forces. This phenomenology is by no means different than that controlling particle deposition at a solid wall [46–50]. Starting from this similarity, in this section we propose a simple mechanistic model that can be used to obtain a

reliable prediction of the capture rate and, at the same time, can easily be implemented in industrially oriented CFD codes. The model is an adaptation of classical deposition models [46,48,49] in which a diffusion-type equation is used to predict particle deposition to a wall by turbulence.

In general, there are three main deposition mechanisms that may act simultaneously: diffusion, impaction, and interception. However, at fluid velocities typical of scrubbing devices and for micron-sized particles such as those considered in the present study, impaction is known to be the dominant capturing mechanism [1]. In this case, the particle deposition rate is assumed to be proportional to the ratio between the mass flux of particles at the deposition surface, J, and the mean bulk concentration of particles, C. Through the definition of a suitable constant of proportionality, usually referred to as the deposition coefficient k_d, the following turbulent transport equation holds:

$$J = k_d C. \tag{23}$$

Given the initial number N_0 of particles released in the carrier fluid subdomain, J and C can be discretized as follows:

$$J = \frac{1}{A}\frac{dN_c(t)}{dt}, \tag{24}$$

$$C = \frac{N_0 - N_c(t)}{V}, \tag{25}$$

where $N_c(t)$ is the number of particles captured by the interface at time t, A is the total surface area of the drops, and V is the volume occupied by the carrier fluid. These definitions yield

$$\frac{dN_c(t)}{dt} = k_d[N_0 - N_c(t)]\frac{A}{V}. \tag{26}$$

Once k_d is known, Eq. (26) can be integrated to yield $N_c(t)$. In particular, for constant A and V,

$$\frac{N_c(t)}{N_0} = 1 - \exp\left(-k_d\frac{A}{V}t\right), \tag{27}$$

where we estimated k_d to scale with the turbulent kinetic energy of the carrier fluid, $\mathcal{K}_T$, based on the observation that capture is driven by the turbulent fluctuations that transport the particles close to the interface. Ideally, it should be $k_d = C\mathcal{K}_T^{1/2}$ with $C \simeq 1$: Through this scaling, the value of k_d can be easily estimated even when Reynolds-averaged Navier-Stokes (RANS)-based commercial flow solvers are used.

In Fig. 6, we show the time evolution of N_c obtained from the simulations for the $\mathrm{St} = 0.1$ and the $\mathrm{St} = 0.8$ particles, and we compare the numerical results with those yielded by Eq. (27). The comparison is proposed for a dimensionless value of the deposition coefficient that satisfies the $k_d \simeq \mathcal{K}_T^{1/2}$ scaling and for a dimensionless value of $\mathcal{K}_T$ computed within a fluid layer of thickness equal to two wall units around the drop (rather than over the entire volume occupied by the carrier fluid). This specific thickness is equal to the volume-averaged value of the Kolmogorov length scale and corresponds to a conservative approximation of the stopping distance of the $St = 0.8$ particles set (the particle stopping distance is the length scale on which we base the choice of the volume-averaging thickness) [46,50]. In this case, we obtain $\mathcal{K}_T^{1/2} \simeq 0.17$. The mean dimensionless value of A/V, also needed in Eq. (27), is equal to 1.3×10^{-3} at the steady state. We readily observe that the increase of N_c is unaffected by particle inertia, as one would expect at such low values of the Stokes number, and follows remarkably well the behavior predicted by the model. We remark here that for the Reynolds number considered in this study, the turbulent kinetic energy averaged over the entire volume occupied by the fluid is $\langle\mathcal{K}_T\rangle \simeq 1.8$, which yields $\langle\mathcal{K}_T\rangle^{1/2} \simeq 1.34$ instead of 0.17. This difference can be ascribed to the deformability of the interface, which acts to damp turbulent fluctuations in the final fluid layer traveled by the particles before being captured by the interfacial forces. Clearly, using $\langle\mathcal{K}_T\rangle$ instead of $\mathcal{K}_T$ in Eq. (27) would significantly worsen the quantitative agreement with the numerical results.

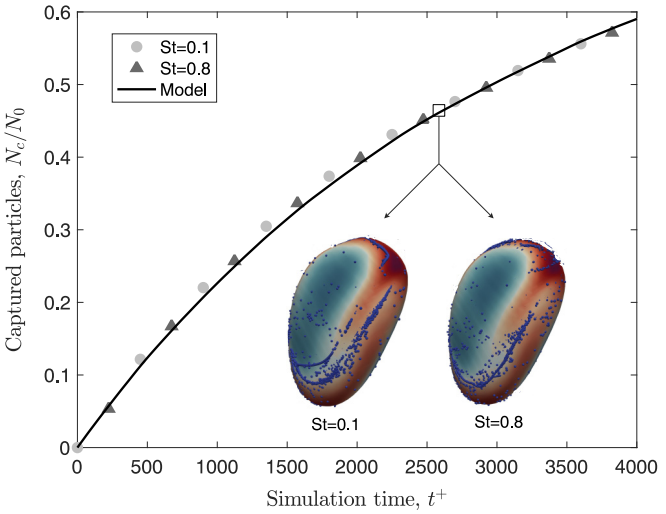

FIG. 6. Time evolution of the number of particles captured by the interface. Symbols refer to simulation results (circles: St = 0.1; triangles: St = 0.8), whereas the solid line refers to the model provided by Eq. (27). The inset shows the instantaneous distribution of the captured particles over the interface of a drop, shown in isolation from the flow domain and colored using the local interface curvature (red: high positive curvature; blue: low negative curvature). Particles appear to sample the same interfacial regions, confirming the secondary role played by inertia.

V. CONCLUSIONS

In this study, we examine the process of particle capture by large deformable drops in turbulent channel flow, and provide a detailed topological characterization of the flow events that control particle adhesion to the drop interface. To simulate the solid-liquid-liquid three-phase flow, we use a state-of-the-art Eulerian-Lagrangian method based on DNS of turbulence coupled with a phase-field model to capture the interface dynamics and Lagrangian tracking of neutrally buoyant, sub-Kolmogorov particles. The drops have the same density and viscosity of the carrier liquid, and the two fluid phases are one-way coupled with the particles. The results discussed in the paper refer to a shear Reynolds number $\mathrm{Re}_\tau = 150$ and values of the Stokes number ranging from $\mathrm{St} = 0.1$ to $\mathrm{St} = 0.8$. To account for possible modifications due to a change of drop deformability, two values of the Weber number were considered, $\mathrm{We} = 0.75$ and 1.5, but no effect of this parameter was observed. Therefore, only results relative to $\mathrm{We} = 0.75$ have been discussed. An extensive analysis of the topological features of the flow events that drive particle transport toward the surface of the drops and lead to particle capture has been conducted. By using topology indicators, we were able to show that particles reach (and adhere to) the interface in regions of positive surface velocity divergence, which are generated by turbulent fluid motions directed towards the interface. These regions of local flow expansion appear to be well correlated with high-enstrophy flow topologies, whereas fluid motions characterized by high strain and high dissipation are generally avoided by the particles. An important role is played by the ability of the interface to deform upon interaction with the neighboring fluid motions, thus giving rise to highly nonuniform curvature and shear stress distributions. In particular, strong tangential stresses are produced on the interface, where the occurrence of localized elongational flows is favored.

Based on the topological characterization of the flow seen by the particles during the capture process, a simple mechanistic model to quantify the fraction of captured particles in time is proposed. This model may be regarded as an attempt to lay useful guidelines for the development of physics-aware predictions of transfer rates in particulate abatement applications, particularly

scrubbing. The proposed model is valid in the limit of noninteracting particles and exploits the proportionality between the mass flux of particles that adhere to the interface and the mean concentration of particles that remains afloat in the bulk of the carrier phase: It is therefore based on a single lumped parameter, i.e., the constant of proportionality between the flux and concentration. In spite of its simplicity, the model is capable of reproducing the time increase of the fraction of captured particles with remarkable accuracy when the deposition coefficient is scaled with the turbulent kinetic energy of the fluid measured within one Kolmogorov length scale from the drop: This scale corresponds to a distance slightly longer than the particle stopping distance, chosen as reference scaling length for the selection of the volume-averaging thickness. This finding can be explained by the fact that in the present flow configuration, particle capture is driven by the turbulent fluctuations in the vicinity of the drop interface. For a mechanistic model to work, it is therefore necessary to incorporate the effect of these near-interface fluctuations on the overall capture coefficient.

The present work focuses primarily on the process of particle capture. A future development (which will be the object of an independent study) is therefore the analysis of the dynamics that characterize the interface-trapped particles as they are driven by both fluid and interfacial stresses. To this aim, it is crucial to consider a system in which particle-particle collisions are taken into account to account for the excluded-volume effects in the regions of particle clustering and to more physically reproduce their distribution over the interface. Also, the numerical setup should be able to mimic the potential effect of trapped particles on interface deformability via local modification (reduction) of the surface tension. The surface-tension gradients so generated might produce additional Marangoni stresses on the interface, which might further change the behavior of the trapped particles. Other issues to be evaluated are the effects due to density and/or viscosity differences among the phases, which were neglected in this study but may definitely induce local modifications of the flow topology in the near-interface regions.

ACKNOWLEDGMENTS

This work has received funding from the European Union's Horizon 2020 research and innovation programme under the Marie Sklodowska-Curie Grant Agreement No. 813948 (COMETE). The authors also gratefully acknowledge funding from the PRIN project "Advanced computations and experiments in turbulent multiphase flow" (Project No. 2017RSH3JY). CINECA (Consorzio inter-universitario per il calcolo automatico, Italy) and VSC (Vienna Scientific Cluster, Austria) are gratefully acknowledged for the generous allowance of computational resources.

[1] H. T. Kim, C. H. Jung, S. N. Oh, and K. W. Lee, Particle removal efficiency of gravitational wet scrubber considering diffusion, interception, and impaction, Environ. Eng. Sci. **18**, 125 (2001).

[2] W. Peukert and C. Wadenpohl, Industrial separation of fine particles with difficult dust properties, Powder Technol. **118**, 136 (2001).

[3] B. C. Meikap, G. Kundu, and M. N. Biswas, Scrubbing of fly-ash laden SO_2 in modified multistage bubble column scrubber, AIChE J. **48**, 2074 (2002).

[4] L. Zhao, M. C. Boufadel, J. Katz, G. Haspel, K. Lee, T. King, and B. Robinson, A new mechanism of sediment attachment to oil in turbulent flows: Projectile particles, Environ. Sci. Tech. **51**, 11020 (2017).

[5] F. Di Natale, C. Carotenuto, L. D'Addio, A. Jaworek, A. Krupa, M. Szudyga, and A. Lancia, Capture of fine and ultrafine particles in a wet electrostatic scrubber, J. Environ. Chem. **3**, 349 (2015).

[6] L. Su, Y. Zhang, Q. Du, X. Dai, J. Gao, P. Dong, and H. Wang, An experimental study on the removal of submicron fly-ash and black carbon in a gravitational wet scrubber with electrostatic enhancement, RSC Adv. **10**, 5905 (2020).

[7] A. D. Dinsmore, M. F. Hsu, M. G. Nikolaides, M. Marquez, A. R. Bausch, and D. A. Weitz, Colloidosomes: Selectively permeable capsules composed of colloidal particles, Science **298**, 1006 (2002).

[8] E. Dickinson, Food emulsions and foams: Stabilization by particles, Curr. Opin. Colloid Interface Sci. **15**, 40 (2010).
[9] K. Stratford, R. Adhikari, I. Pagonabarraga, J. C. Desplat, and M. E. Cates, Colloidal jamming at interfaces: A route to fluid-bicontinuous gels, Science **309**, 2198 (2005).
[10] C. Goniva, Z. Tuković, C. Feilmayr, and S. Pirker, Direct numerical simulation of turbulent flows laden with droplets or bubbles, Prog. Comput. Fluid Dyn. **10**, 265 (2010).
[11] N. Rafidi, F. Brogaard, L. Chen, R. Håkansson, and A. Tabikh, CFD and experimental studies on capture of fine particles by liquid droplets in open spray towers, Sustain. Environ. Res. **28**, 382 (2018).
[12] S. Elghobashi, Direct numerical simulation of turbulent flows laden with droplets or bubbles, Annu. Rev. Fluid Mech. **51**, 217 (2019).
[13] B. P. Binks, Particles as surfactants similarities and differences, Curr. Opin. Colloid Interface Sci. **7**, 21 (2002).
[14] B. J. Park and D. Lee, Particles at fluid-fluid interfaces: From single-particle behavior to hierarchical assembly of materials, MRS Bull. **39**, 1089 (2014).
[15] C. Gu and L. Botto, Direct calculation of anisotropic surface stresses during deformation of a particle-covered drop, Soft Matter **12**, 705 (2016).
[16] G. Lecrivain, R. Yamamoto, U. Hampel, and T. Taniguchi, Direct numerical simulation of a particle attachment to an immersed bubble, Phys. Fluids **28**, 083301 (2016).
[17] G. Pozzetti and B. Peters, A multiscale DEM-VOF method for the simulation of three-phase flows, Int. J. Multiphase Flow **99**, 186 (2018).
[18] X. Sun and M. Sakai, Three-dimensional simulation of gas-solid-liquid flows using the DEM-VOF method, Chem. Eng. Sci. **134**, 531 (2015).
[19] M. S. Dodd and L. Jofre, Small-scale flow topologies in decaying isotropic turbulence laden with finite-size droplets, Phys. Rev. Fluids **4**, 064303 (2019).
[20] Q. Li, M. Abbas, and J. F. Morris, Particle approach to a stagnation point at a wall: Viscous damping and collision dynamics, Phys. Rev. Fluids **5**, 104301 (2020).
[21] C. Gu and L. Botto, FIPI: A fast numerical method for the simulation of particle-laden fluid interfaces, Comput. Phys. Commun. **256**, 107447 (2020).
[22] G. Soligo, A. Roccon, and A. Soldati, Effect of surfactant-laden droplets on turbulent flow topology, Phys. Rev. Fluids **5**, 073606 (2020).
[23] M. S. Chong, A. E. Perry, and B. J. Cantwell, A general classification of three-dimensional flow fields, Phys. Fluids A: Fluid Dyn. **2**, 765 (1990).
[24] Y. Li, J. L. Choi, and J. Kim, A phase-field fluid modeling and computation with interfacial profile correction term, Commun. Nonlin. Sci. **30**, 84 (2016).
[25] Y. Zhang and W. Ye, A flux-corrected phase-field method for surface diffusion, Commun. Comput. Phys. **22**, 422 (2017).
[26] G. Soligo, A. Roccon, and A. Soldati, Mass-conservation-improved phase field methods for turbulent multiphase flow simulation, Acta Mech. **230**, 683 (2019).
[27] L. Scarbolo, F. Bianco, and A. Soldati, Coalescence and breakup of large droplets in turbulent channel flow, Phys. Fluids **27**, 073302 (2015).
[28] A. Roccon, M. De Paoli, F. Zonta, and A. Soldati, Viscosity-modulated breakup and coalescence of large drops in bounded turbulence, Phys. Rev. Fluids **2**, 083603 (2017).
[29] H. Ding, P. D. Spelt, and C. Shu, Diffuse interface model for incompressible two-phase flows with large density ratios, J. Comput. Phys. **226**, 2078 (2007).
[30] R. Ettelaie and S. V. Lishchuk, Detachment force of particles from fluid droplets, Soft Matter **11**, 4251 (2015).
[31] V. E. Badalassi, H. D. Ceniceros, and S. Banerjee, Computation of multiphase systems with phase field models, J. Comput. Phys. **190**, 371 (2003).
[32] P. Yue, J. Feng, C. Liu, and J. Shen, A diffuse-interface method for simulating two-phase flows of complex fluids, J. Fluid Mech. **515**, 293 (2004).
[33] M. Di Renzo, P. L. Johnson, M. Bassenne, L. Villafañe, and J. Urzay, Mitigation of turbophoresis in particle-laden turbulent channel flows by using incident electric fields, Phys. Rev. Fluids **4**, 124303 (2019).

[34] J. G. M. Kuerten and A. W. Vreman, Effect of droplet interaction on droplet-laden turbulent channel flow, Phys. Fluids **27**, 053304 (2015).
[35] C. Marchioli, A. Soldati, J. G. M. Kuerten, B. Arcen, A. Taniere, G. Goldensoph, K. D. Squires, M. F. Cargnelutti, and L. M. Portela, Statistics of particle dispersion in direct numerical simulations of wall-bounded turbulence: Results of an international collaborative benchmark test, Int. J. Multiphase Flow **34**, 879 (2008).
[36] G. Soligo, A. Roccon, and A. Soldati, Coalescence of surfactant-laden drops by phase field method, J. Comput. Phys. **376**, 1292 (2019).
[37] P. Than, L. Preziosi, D. Josephl, and M. Arney, Measurement of interfacial tension between immiscible liquids with the spinning road tensiometer, J. Colloid Interface Sci. **124**, 552 (1988).
[38] F. Magaletti, F. Picano, M. Chinappi, L. Marino, and C. M. Casciola, The sharp-interface limit of the Cahn-Hilliard/Navier-Stokes model for binary fluids, J. Fluid Mech. **714**, 95 (2013).
[39] A. E. Perry and M. S. Chong, A description of eddying motions and flow patterns using critical-point concepts, Annu. Rev. Fluid Mech. **19**, 125 (1987).
[40] M. Picciotto, C. Marchioli, and A. Soldati, Characterization of near-wall accumulation regions for inertial particles in turbulent boundary layers, Phys. Fluids **17**, 098101 (2005).
[41] H. M. Blackburn, N. N. Mansour, and B. J. Cantwell, Topology of fine-scale motions in turbulent channel flow, J. Fluid Mech. **310**, 269 (1996).
[42] F. De Vita, M. E. Rosti, S. Caserta, and L. Brandt, On the effect of coalescence on the rheology of emulsions, J. Fluid Mech. **880**, 969 (2019).
[43] M. E. Rosti, F. De Vita, and L. Brandt, Numerical simulations of emulsions in shear flows, Acta Mech. **230**, 667 (2019).
[44] S. De, J. Kuipers, E. A. J. F. Peters, and J. T. Padding, Viscoelastic flow simulations in random porous media, J. Non-Newton. Fluid **248**, 50 (2017).
[45] L. Scarbolo and A. Soldati, Turbulence modulation across the interface of a large deformable drop, J. Turbul. **14**, 27 (2013).
[46] S. Friedlander and H. Johnstone, Deposition of suspended particles from turbulent gas streams, Ind. Eng. Chem. **49**, 1151 (1957).
[47] J. Cleaver and B. Yates, A sub layer model for the deposition of particles from a turbulent flow, Chem. Eng. Sci. **30**, 983 (1975).
[48] L. B. Cousins and G. F. Hewitt, Liquid phase mass transfer in annular two-phase flow, UKAEA Report No. AERE-R 5657 (UK Atmoic Energy Authority, Harwell, Oxfordshire (UK), 1968).
[49] A. Soldati and P. Andreussi, The influence of coalescence on droplet transfer in vertical annular flow, Chem. Eng. Sci. **51**, 353 (1996).
[50] A. Soldati and C. Marchioli, Physics and modeling of turbulent particle deposition and entrainment: Review of a systematic study, Int. J. Multiphase Flow **35**, 827 (2009).